SOLAR CELLS

Ion-modulated radical doping of spiro-OMeTAD for more efficient and stable perovskite solar cells

Tiankai Zhang[1]†, Feng Wang[1]*†, Hak-Beom Kim[2], In-Woo Choi[2], Chuanfei Wang[3], Eunkyung Cho[4], Rafal Konefal[5], Yuttapoom Puttisong[1], Kosuke Terado[6], Libor Kobera[5], Mengyun Chen[1], Mei Yang[1], Sai Bai[1], Bowen Yang[7,8], Jiajia Suo[7,8], Shih-Chi Yang[9], Xianjie Liu[3], Fan Fu[9], Hiroyuki Yoshida[6,10], Weimin M. Chen[1], Jiri Brus[5], Veaceslav Coropceanu[4], Anders Hagfeldt[7,8], Jean-Luc Brédas[4], Mats Fahlman[3], Dong Suk Kim[2], Zhangjun Hu[1], Feng Gao[1]*

Record power conversion efficiencies (PCEs) of perovskite solar cells (PSCs) have been obtained with the organic hole transporter 2,2′,7,7′-tetrakis(*N*,*N*-di-*p*-methoxyphenyl-amine)9,9′-spirobifluorene (spiro-OMeTAD). Conventional doping of spiro-OMeTAD with hygroscopic lithium salts and volatile 4-*tert*-butylpyridine is a time-consuming process and also leads to poor device stability. We developed a new doping strategy for spiro-OMeTAD that avoids post-oxidation by using stable organic radicals as the dopant and ionic salts as the doping modulator (referred to as ion-modulated radical doping). We achieved PCEs of >25% and much-improved device stability under harsh conditions. The radicals provide hole polarons that instantly increase the conductivity and work function (WF), and ionic salts further modulate the WF by affecting the energetics of the hole polarons. This organic semiconductor doping strategy, which decouples conductivity and WF tunability, could inspire further optimization in other optoelectronic devices.

Metal halide perovskites have achieved impressive power conversion efficiencies (PCEs) in both single-junction (*1*–*6*) and tandem solar cells (*7*, *8*). However, a key challenge limiting their practical application is the trade-off between high efficiency and high stability, an issue determined by not only the perovskite materials (*9*) but also the charge transport layers (*10*). Currently, most high-performance perovskite solar cells (PSCs) with >24% PCE are based on the benchmark hole transport layer (HTL) spiro-OMeTAD doped by lithium bis(trifluoromethane)sulfonimide (LiTFSI) and 4-*tert*-butylpyridine (tBP) (*11*–*13*), a process that limits the stability of these high-efficiency PSCs.

Conventional spiro-OMeTAD doping (Fig. 1A, top) involves LiTFSI to facilitate the generation of spiro-OMeTAD$^{\bullet+}$TFSI$^-$ radicals and tBP to improve dopants' solubility and film morphology (*14*). This recipe usually requires an in situ oxidization process for a period of 10 to 24 hours in air to reach the optimal conductivity and work function (WF) (*15*). However, because of the low doping efficiency of this process, a large amount of dopants and additives (~56 mol % LiTFSI and ~330 mol % tBP) are required to generate ~10 mol % radicals (*16*). The residual LiTFSI, tBP, and by-products (e.g., Li_xO_y) are not only diffusible (*17*) but also sensitive to humidity and heat (*18*, *19*), negatively affecting device stability.

In addition, the complex in situ oxidation process makes it challenging to understand the mechanism of conventional spiro-OMeTAD doping, which limits further development of stable HTLs with high PCEs. Several efforts addressing the spiro-OMeTAD stability issue have focused on the hygroscopic lithium salt. For example, a CO_2 gas-forming treatment was recently used to remove the hygroscopic lithium species (*20*). Less hygroscopic dopants, including metallic salts (*21*–*23*), protic ionic liquids (*24*), and ex situ synthesized spiro-OMeTAD$^{2\bullet+}$(TFSI$^-$)$_2$ radicals (*25*, *26*), have also been used to replace the oxidant LiTFSI. Such doping usually requires the addition of volatile tBP, whose role in the doping process has been controversial (*27*, *28*). In particular, tBP would react with radicals and coordinate with LiTFSI to form by-products (Fig. 1A, top), which not only negatively affects device performance but also prevents a full understanding of the spiro-OMeTAD doping mechanism.

We developed a stable doping strategy for instant and effective doping of spiro-OMeTAD, which we call ion-modulated (IM) radical doping (Fig. 1A, bottom), that relies on two components. One is the presynthesized stable spiro-OMeTAD$^{2\bullet+}$(TFSI$^-$)$_2$ radical (synthesis and characterizations in figs. S1 and S2), which acts as the main dopant to improve conductivity and WF. The second is the ionic salt 4-*tert*-butyl-1-methylpyridinium bis(trifluoromethylsulfonyl)imide (TBMP$^+$TFSI$^-$) to further modulate the WF. In this doping strategy, the localized ionic environment created by the ionic salt was used to manipulate the energetics of the hole polarons and decouple the conductivity and WF tunability. The doped spiro-OMeTAD based on our IM radical doping strategy delivered PSCs simultaneously with high efficiency (PCE > 25%) and high stability (T_{80} for ~1200 hours under 70 ± 5% relative humidity (RH) and T_{80} for ~800 hours under 70° ± 3°C without encapsulation), minimizing the trade-off between efficiency and stability of PSCs. In addition, the IM radical doping strategy provides a facile yet effective approach to separately optimize the conductivity and WF of organic semiconductors for a variety of optoelectronic applications.

PSC performance based on IM radical–doped spiro-OMeTAD

We first compared the distinctive effects of conventional and IM radical doping of spiro-OMeTAD using $(FAPbI_3)_{0.99}(MAPbBr_3)_{0.01}$ (FA, formamidinium; MA, methylammonium) PSCs with an SnO_2 electron transport layer (ETL) (fig. S3) (*12*). The conventional spiro-OMeTAD doping process requires an oxidation time of ~24 hours to reach the optimized PCE of 22.2% (Fig. 1B, fig. S4A, and table S1). The gradual improvement in device performance with increasing oxidation time is consistent with the conductivity increase (fig. S5A) that resulted from the continuous generation of spiro-OMeTAD$^{\bullet+}$TFSI$^-$ radicals, as evidenced by the ultraviolet–visible–near-infrared (UV-Vis-NIR) absorption spectra (fig. S5B) (*29*, *30*).

In our IM spiro-OMeTAD doping strategy, the first additive consists of presynthesized spiro-OMeTAD$^{2\bullet+}$(TFSI$^-$)$_2$ (*31*, *32*), which can be immediately converted into spiro-OMeTAD$^{\bullet+}$TFSI$^-$ monoradicals through comproportionation with the neutral spiro-OMeTAD (*25*):

$$\text{spiro-OMeTAD} + \text{spiro-OMeTAD}^{2\bullet+}(\text{TFSI}^-)_2 \rightarrow 2\ \text{spiro-OMeTAD}^{\bullet+}\text{TFSI}^- \quad (1)$$

We note that more radical cations (and hence a higher conductivity) are obtained at lower dopant levels using the current approach than using LiTFSI, as indicated by absorption spectra and conductivity measurements (fig. S5). Upon the incorporation of radicals, the device performance improved relative to undoped spiro-OMeTAD (fig. S4B), and an optimal performance was reached with the doping radical ratio of ~14 mol % (calculated to the ratio of monoradicals). However, compared to a high open-circuit voltage (V_{oc}) of 1.15 V achieved with the conventional doping recipe, the optimized V_{oc} of spiro-OMeTAD doped with radicals was 1.04 V (Fig. 1B).

[1]Department of Physics, Chemistry and Biology (IFM), Linköping University, 58183 Linköping, Sweden. [2]Korea Institute of Energy Research (KIER), Ulsan, Republic of Korea. [3]Laboratory of Organic Electronics, Department of Science and Technology, Linköping University, 60174 Norrköping, Sweden. [4]Department of Chemistry and Biochemistry, University of Arizona, Tucson, AZ 85721, USA. [5]Institute of Macromolecular Chemistry of the Czech Academy of Sciences, 162 06 Prague 6, Czech Republic. [6]Graduate School of Engineering, Chiba University, 1-33 Yayoi-cho, Inage-ku, Chiba 263-8522, Japan. [7]Laboratory of Photomolecular Science (LSPM), École Polytechnique Fédérale de Lausanne, CH-1015 Lausanne, Switzerland. [8]Department of Chemistry, Ångström Laboratory, Uppsala University, SE-751 20 Uppsala, Sweden. [9]Laboratory for Thin Films and Photovoltaics, Empa–Swiss Federal Laboratories for Materials Science and Technology, CH-8600 Duebendorf, Switzerland. [10]Molecular Chirality Research Center, Chiba University, 1-33 Yayoi-cho, Inage-ku, Chiba 263-8522, Japan. *Corresponding author. Email: feng.wang@liu.se (F.W.); feng.gao@liu.se (F.G.)
†These authors contributed equally to this work.

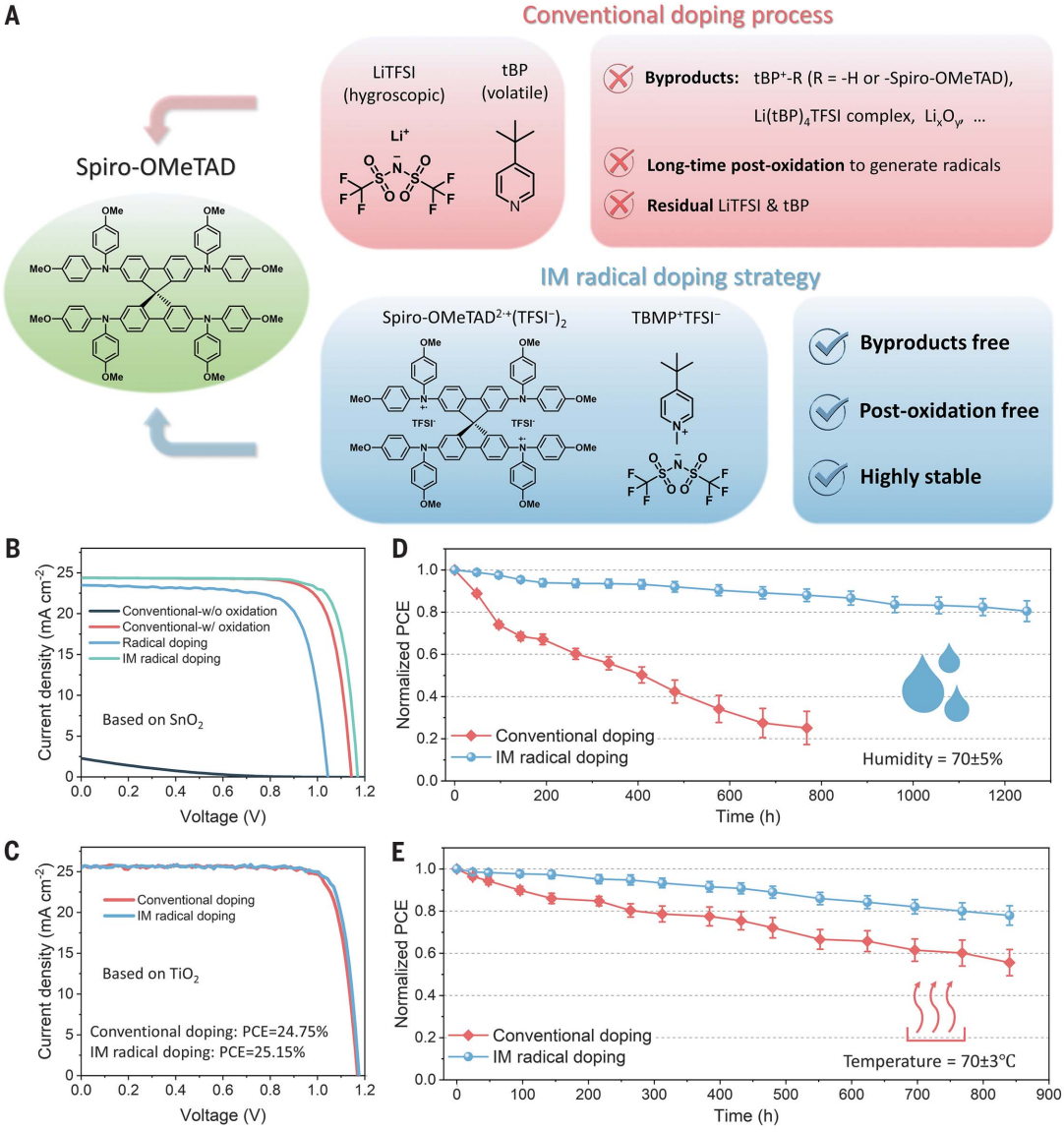

Fig. 1. Comparison of perovskite solar cells (PSCs) based on the conventional and ion-modulated (IM) radical doping strategies. (**A**) Illustration of the complex in situ reaction processes in the conventional doping process (top) and the clean, instant IM radical doping strategy (bottom) of spiro-OMeTAD. The radical and ionic salt were dissolved in 1,1,2,2-tetrachloroethane. (**B**) Current density–voltage (*J-V*) curves of PSCs (SnO_2 electron transport layer) based on conventional doping, radical doping, and IM radical doping of spiro-OMeTAD. (**C**) *J-V* curves of PSCs (mesoporous TiO_2 electron transport layer) based on conventional and IM radical doping of spiro-OMeTAD. (**D** and **E**) PCE tracking of unencapsulated PSCs based on conventional and IM radical doping of spiro-OMeTAD under 70 ± 5% humidity (D) and 70 ± 3°C thermal aging (E). Error bars denote SD.

Upon addition of the second additive (ionic salt, $TBMP^+TFSI^-$), the V_{oc} of the solar cells increased and a V_{oc} of 1.17 V was achieved with 20 mol % $TBMP^+TFSI^-$. The resulting PCE of 23.4 % was even higher than that based on the conventional doping (Fig. 1B). Further increasing the $TBMP^+TFSI^-$ content led to a decrease in the fill factor (FF) (fig. S4C and table S2) possibly because of ion aggregation (fig. S6).

The high V_{oc} of the optimized devices was also consistent with the values of electroluminescence external quantum efficiency (EL_{EQE}), which increased from 0.05% to 5.4% upon the addition of 20 mol % $TBMP^+TFSI^-$ into the HTL (fig. S7), indicating reduced nonradiative recombination. Remarkably, based on the meso-TiO_2 scaffold with $FAPbI_3$ as the active layer, the IM radical doping of spiro-OMeTAD delivered a PCE of 25.1% (table S3, certified 25.0% in fig. S8), which was again higher than that of the control device with conventionally doped spiro-OMeTAD (Fig. 1C). The PCE statistics demonstrated that the IM radical doping strategy, which did not involve a post-oxidation process, was more controllable than the conventional doping process (fig. S9).

Because the IM radical doping strategy completely removed the need to use hygroscopic LiTFSI and volatile tBP, an improvement in device stability can be expected. We systematically compared the device stability with IM radical doping versus conventional doping as a function of RH, heat, and illumination. Relative to the conventional doping of spiro-OMeTAD, the IM radical doping strategy extended the T_{80} of PSCs (unencapsulated) from ~96 to ~1240 hours under high RH of ~70 ± 5% (Fig. 1D and fig. S10), and T_{80} from ~264 to ~796 hours under ~70° ± 3°C (Fig. 1E and fig. S11). The improved device stability with the IM radical–doped HTL was ascribed to not only the improved stability of HTL but also the prevention of phase and thermal degradation of the perovskite active layer under high RH and under heat stress, as evidenced from optical images (fig. S12) and x-ray diffraction results (figs. S13 and S14) of the degraded devices.

Scanning electron microscopy (SEM) images provided more details of the protection effect from the spiro-OMeTAD HTL based on IM radical doping. A large number of pinholes were observed in degraded devices based on the conventionally doped HTLs, implying that LiTFSI residuals absorbed moisture and that tBP volatilized gradually. Both effects accelerated the degradation of the perovskite active layer (figs. S15 and S16). In contrast, the devices based on the IM radical doping strategy maintained a compact and uniform morphology after long-term exposure to high RH and

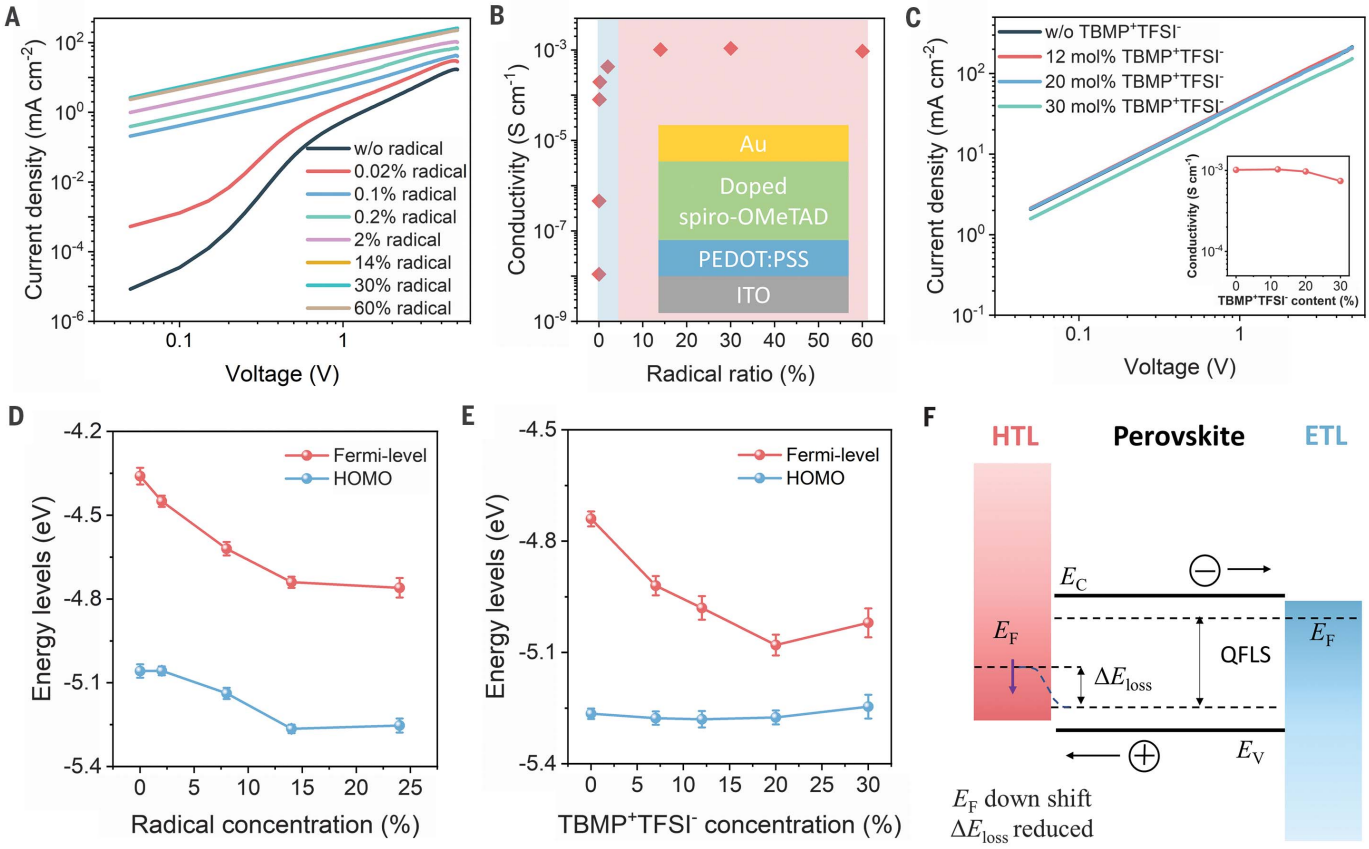

Fig. 2. Effects of radicals and ionic salts on conductivity and energetics. (**A** and **B**) *J-V* curves of the hole-only devices (A) and conductivity of the spiro-OMeTAD films doped with different radical amounts (B). Inset of (B) shows the structure of the hole-only devices. (**C**) *J-V* curves of the hole-only devices with 14 mol % radicals and different amounts of $TBMP^+TFSI^-$. The inset shows conductivity. (**D** and **E**) Fermi-level and HOMO onsets of the spiro-OMeTAD films doped with different radical amounts (D) and different $TBMP^+TFSI^-$ amounts (14 mol % radicals) (E). Error bars denote SD. (**F**) Illustration of the band alignment between the perovskite layer and the HTL with different WF values.

thermal stress (figs. S15 and S17), protecting the perovskite layer underneath. In addition, under maximum power point (MPP) tracking, the PCEs of PSCs based on conventional doping decayed to ~85% after 500 hours of continuous illumination. Devices based on the IM radical doping strategy maintained ~95% of the initial PCE after the same operational time (fig. S18), similar to that of devices using inorganic HTLs (*33*, *34*) or undoped polymer HTLs (*35*).

The roles of radicals and ionic salts on spiro-OMeTAD doping

Our IM radical doping strategy provided an instantly effective and stable doping of spiro-OMeTAD. In addition, this simple process allowed us to decouple and investigate the fundamental functions of additives (radicals and ionic salts). We focused on two physical parameters that are key to the effectiveness of the HTL: conductivity and energy levels [including both WF and ionization energy (IE)].

To investigate the HTL conductivity, we used hole-only devices with the structure ITO/PEDOT:PSS/doped spiro-OMeTAD/Au [ITO, indium tin oxide; PEDOT, poly(3,4-ethylenedioxythiophene); PSS, polystyrene sulfonate]. The effects of organic radicals on the film conductivity (Fig. 2, A and B) showed two distinct stages as a function of an increasing amount of organic radicals. There was initially an extremely high doping efficiency with a small doping ratio of radicals (<2 mol %; Fig. 2B, light blue area), which suggested efficient hole polaron generation. In particular, 0.1 mol % of radicals could increase the conductivity of the film by almost four orders of magnitude, from 1.10×10^{-8} S cm^{-1} to 8.03×10^{-5} S cm^{-1}. This increase could be attributed to the filling of deep trap states by dopant-generated charge carriers, which would bring increased carrier concentration as well as higher carrier mobility (*36*).

For higher doping concentrations, the hole-only current density exhibited a linear dependence over the entire voltage range from 0 V to 5 V, indicative of a high hole concentration in the system. In the second stage (doping ratio from 2 mol % to 60 mol %, marked by the light red area), the doping efficiency nearly saturated and the conductivity peaked at ~1.00×10^{-3} S cm^{-1} at ~14 mol % radicals (Fig. 2B). This doping saturation phenomenon was consistent with previous reports in other organic semiconductor systems and is ascribed to the increase in energetic disorder induced by long-range Coulomb interactions when increasing the number of dopants (*37*). The addition of the $TBMP^+TFSI^-$ ionic salt had negligible effects on the film conductivity over a wide range of concentrations (up to 20 mol %) (Fig. 2C), beyond which a slight decrease in film conductivity was observed, possibly because of the aforementioned phase aggregation and increased disorder in the film (see below).

In addition to conductivity, the energy level alignment at the HTL interface is another parameter that is critically important to device performance. An optimal energy level of the HTL helps to facilitate hole extraction and eliminate interfacial nonradiative recombination, contributing to high device performance (especially high V_{oc}). We investigated the impact of the radicals on the relevant energy levels by ultraviolet photoelectron spectroscopy (UPS). For the pristine spiro-OMeTAD, the ionization energy (IE) was 5.08 eV, which according to Koopmans' theorem (*38*) corresponds to the energy of the highest occupied molecular orbital (HOMO), and the WF was 4.36 eV (fig. S19A). The density functional theory (DFT)

results showed that the IE of an isolated spiro-OMeTAD molecule was ~5.46 eV, and this value decreased to 5.03 eV when the calculations were performed by taking into account an effective medium with a dielectric constant of 2.4 (fig. S20).

With increasing amounts of radicals, both IE and WF increased (Fig. 2D). A more detailed comparison revealed that the difference between WF and IE decreases along with increasing dopant concentration (Fig. 2D), emphasizing the extent to which the Fermi level moves toward the HOMO level, which is a key signature of p-doping. Combining the conductivity results in Fig. 2B, we noticed that a radical concentration of >2 mol % could affect the energy levels of the film despite almost no improvement in conductivity. The shift of energetic levels saturated at ~14 mol % radical doping, which is due to the limit in charge transfer and hole generation (*37*).

Based on the 14 mol % radical–doped system, we further assessed the effect of the $TBMP^+TFSI^-$ ionic salt on the film energy levels. In contrast to the simultaneous change of the HOMO level and WF upon the addition of radicals, the ionic salt increased the WF to 5.08 eV with 20 mol % $TBMP^+TFSI^-$ but had a negligible effect on the HOMO levels (Fig. 2E and fig. S19B). The slightly decreased WF with 30% $TBMP^+TFSI^-$ was ascribed to the effects of ion aggregation (fig. S6). As such, the addition of $TBMP^+TFSI^-$ breaks the doping limit of radical doping, resulting in a Fermi level that is very close to the HOMO level (the difference is as small as 0.12 eV, a value much smaller than those obtained in traditional organic semiconductor doping). The promoted doping efficiency after $TBMP^+TFSI^-$ incorporation was also confirmed by the increased carrier concentration, as indicated from a Mott-Schottky analysis (fig. S21).

In PSCs, as long as the HOMO energy of the HTL remains above the valence band of perovskites, it has little impact on the device V_{oc} value. For example, different HTLs with HOMO energies between −5.2 and −5.4 eV have almost the same *J-V* curves (*39*). Within a suitable HOMO energy range, an optimal WF of the HTL aligned with the quasi–Fermi level (QFL) of the perovskite active layer is critical to minimizing the voltage loss (*40*, *41*). As illustrated in Fig. 2F, the increase of the WF by the $TBMP^+TFSI^-$ reduced the hole extraction barrier between the perovskite and the IM radical–doped HTL film. This change enables a high QFL splitting in the perovskites under illumination by eliminating the interfacial nonradiative recombination loss. Thus, this WF modulation by the ionic salt is important, as this V_{oc} improvement made it possible for the device based on our IM radical doping strategy to reach the performance comparable to that based on conventional doping (refer to Fig. 1, B and C).

From these conductivity and energy level investigations, the different functions assumed by the organic radicals and ionic salts become clear. The radicals enhance the conductivity and affect the energy levels (both HOMO and WF); the ionic salts further optimize the WF and contribute to optimal V_{oc} values in the devices.

The effectiveness of the radicals as a means of tuning the conductivity and energy levels can be understood with a charge transfer model between neutral spiro-OMeTAD and the spiro-$OMeTAD^{\bullet+}TFSI^-$ radical. For neutral spiro-OMeTAD, the Fermi level (E_F) corresponds to an energy about midway between the lowest unoccupied molecular orbital (LUMO) and HOMO levels (fig. S20). The low film conductivity in the absence of dopant can be understood by poor film crystallinity and low charge carrier concentrations, which are determined by thermal excitation of charge carriers from HOMO to LUMO levels.

Upon radical doping, spiro-$OMeTAD^{\bullet+}TFSI^-$ provides additional electronic states (*42*) (figs. S22 to S24)—specifically, bound hole states corresponding to singly unoccupied molecular orbital (SUMO) levels stabilized by Coulombic attraction from the $TFSI^-$ counterion. Electron transfer from neutral spiro-OMeTAD (host) to spiro-$OMeTAD^{\bullet+}TFSI^-$ radical complex (dopant) leads to the generation of free hole polarons and increases the conductivity (Fig. 3A). Concurrently, the hole filling of the transport states downshifts the Fermi level and increases the WF (Fig. 2D) (*43*, *44*).

The mechanism of ionic salts modulating spiro-OMeTAD doping

We now turn to a discussion of how ionic salts can further tune the WF. We did not observe oxidation or reduction between ionic salts and neutral spiro-OMeTAD/spiro-$OMeTAD^{\bullet+}TFSI^-$ (figs. S25 and S26). A straightforward possibility for inducing the WF change is the introduction of a macroscopic dipole, which could be induced either by a particular spiro-OMeTAD orientation (*45*) or by an interfacial $TBMP^+TFSI^-$ accumulation (*46*). We excluded the former on the basis of the grazing-incidence wide-angle x-ray scattering (GIWAXS) results (fig. S27), which indicated neither stacking mode change nor crystallization amelioration upon addition of $TBMP^+TFSI^-$. The latter could be ruled out because time-of-flight secondary ion mass spectroscopy (TOF-SIMS) measurements showed a uniform distribution of S^-, $C_4H_9^-$, $C_5H_4N^-$, and CF_3^- across the entire HTL (fig. S28), indicating the absence of surface dipoles formed by $TBMP^+TFSI^-$. In addition, the incorporation of ionic salts increased the WF more than its effects on the IE (Fig. 2D), further ruling out the possibility of the surface-dipole effect.

The exclusion of macroscopic dipole formation motivated us to understand the WF tuning mechanism at the molecular level. Both radicals and salts are ionic, so Coulomb interactions among them are to be expected and would affect their frontier orbital energetics. Details on the Coulomb interactions between the ionic salts and radicals were obtained from both high-resolution liquid and solid-state nuclear magnetic resonance (hr- and ss-NMR, respectively) spectroscopies (Fig. 3B). Although NMR spectroscopy cannot provide direct information on radicals given the strong interactions of unpaired electrons with NMR active nuclei, comparison between different samples provided useful information on the interactions in our mixture. We observed electron transfer between spiro-$OMeTAD^{\bullet+}TFSI^-$ and spiro-OMeTAD, in that all ^1H signals (labeled a to f) of spiro-OMeTAD hr-NMR spectra were broadened after the addition of spiro-$OMeTAD^{\bullet+}TFSI^-$ (Fig. 3B and fig. S29). The broad signal half-widths suggested that spiro-$OMeTAD^{\bullet+}TFSI^-$ and neutral spiro-OMeTAD were near each other and mutually exchanging electrons, which could be attributed to π-π stacking between fluorene moieties of spiro-OMeTAD and spiro-$OMeTAD^{\bullet+}TFSI^-$ (*47*, *48*). However, the ^1H NMR signals of spiro-OMeTAD d+e+f were more broadened while the b and c peaks were only slightly affected, indicating that the electron exchange between spiro-OMeTAD and spiro-$OMeTAD^{\bullet+}TFSI^-$ influenced the molecules only partially on the fluorene part (*49*).

Upon addition of $TBMP^+TFSI^-$ into the spiro-OMeTAD and spiro-$OMeTAD^{\bullet+}TFSI^-$ mixture, the ^1H NMR signals from all aromatic protons (b, c, and d+e+f) of spiro-OMeTAD nearly disappeared (Fig. 3B). This indicated more effective electron exchange between spiro-OMeTAD and spiro-$OMeTAD^{\bullet+}TFSI^-$ in the presence of the $TBMP^+TFSI^-$ salt. Because direct interactions between $TBMP^+TFSI^-$ and spiro-OMeTAD were negligible (fig. S29A), we attributed the effect of $TBMP^+TFSI^-$ on the ^1H hr-NMR signals (Fig. 3B) to Coulomb interactions between spiro-$OMeTAD^{\bullet+}TFSI^-$ and $TBMP^+TFSI^-$, which enhanced charge transfer between spiro-OMeTAD and spiro-$OMeTAD^{\bullet+}TFSI^-$ in the presence of the $TBMP^+TFSI^-$ salt. The emergence of these interactions is consistent with the shift and narrowing of the ^{19}F ss-NMR peak of $TFSI^-$ (fig. S30).

A complementary electron paramagnetic resonance (EPR) study from 77 K to room temperature demonstrated a Lorentzian broadening of EPR spectra in our radical-doped spiro-OMeTAD (for samples both with and without $TBMP^+TFSI^-$) (Fig. 3C and figs. S31 and S32). We attributed this effect to the dynamic broadening due to the electron self-exchange between the neutral spiro-OMeTAD and spiro-$OMeTAD^{\bullet+}TFSI^-$ radical. Within the intermediate exchange rate limit, the EPR broadening upon $TBMP^+TFSI^-$ incorporation was attributed to the increased electron transfer rate between the neutral spiro-OMeTAD and

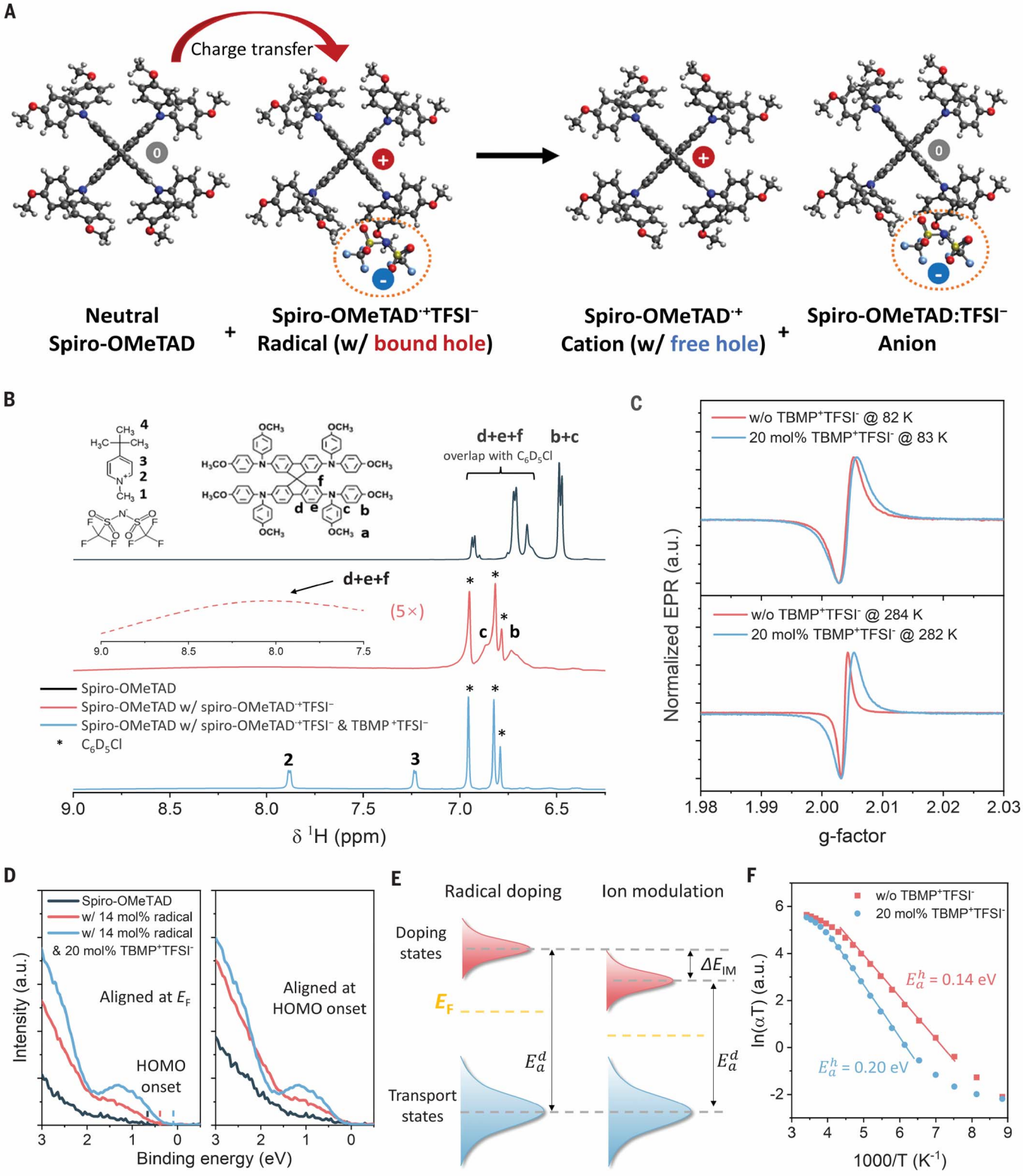

Fig. 3. Molecular-level doping mechanisms of the IM radical doping. (**A**) Illustration of the charge transfer and doping mechanisms with spiro-OMeTAD$^{\cdot+}$TFSI$^-$ radicals. (**B**) ^{1}H hr-NMR spectra of spiro-OMeTAD (black line), spiro-OMeTAD/spiro-OMeTAD$^{\cdot+}$TFSI$^-$ mixture without TBMP$^+$TFSI$^-$ (red line; inset shows magnified view of d+e+f peak in the range of 9 to ~7.5 ppm), and spiro-OMeTAD/spiro-OMeTAD$^{\cdot+}$TFSI$^-$ mixture with TBMP$^+$TFSI$^-$ (blue line) in the range 9 to 6.25 ppm. (Peaks b, c, and d+e+f refer to the aromatic protons signal.) (**C**) EPR signals of doped spiro-OMeTAD (14 mol % radicals) with and without TBMP$^+$TFSI$^-$ at low temperature and room temperature. (**D**) Zoom-in spectra near the valence band of neutral spiro-OMeTAD, 14 mol % radical–doped spiro-OMeTAD film, and 14 mol % radical and 20 mol % TBMP$^+$TFSI$^-$–doped spiro-OMeTAD films. (**E**) Illustration of ionic salts' effect on WF modulation in the framework of the IM radical doping strategy. (**F**) Temperature-dependent conductivity evolution of doped spiro-OMeTAD (14 mol % radicals) with and without TBMP$^+$TFSI$^-$.

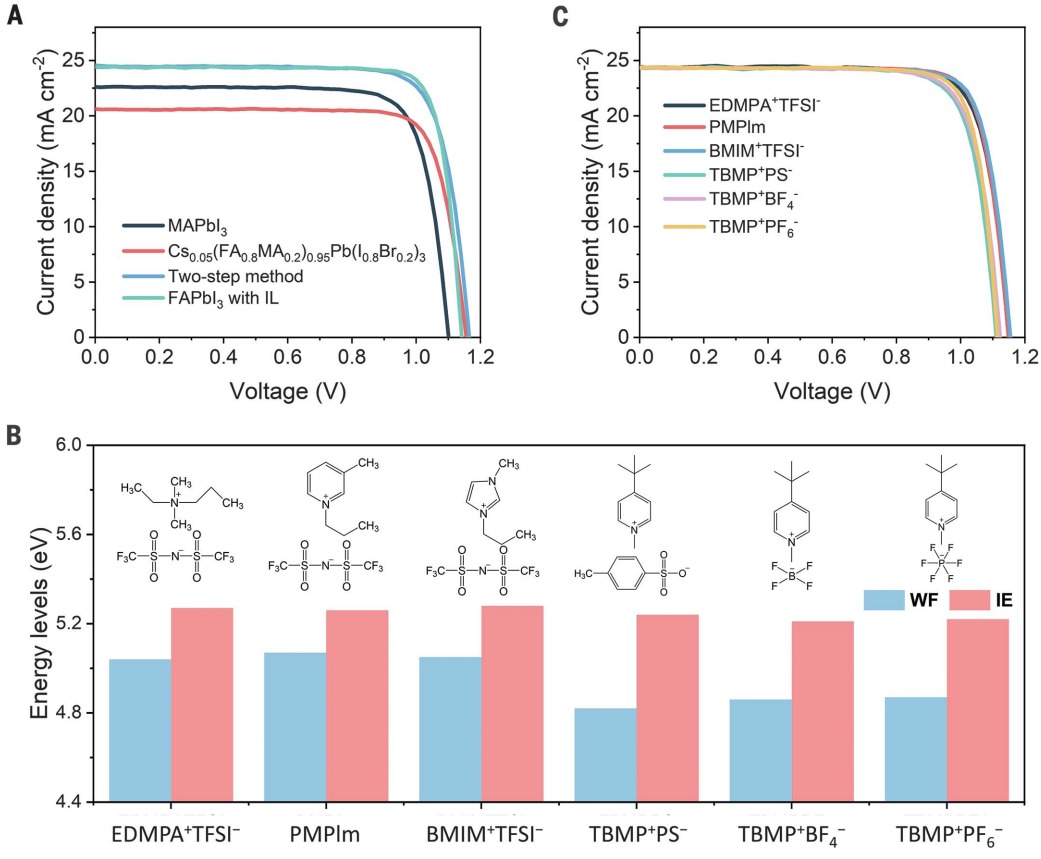

Fig. 4. Generality of the IM radical doping strategy. (**A**) *J-V* curves of different PSCs based on spiro-OMeTAD HTL following the IM radical doping strategy. (**B**) Molecular structures of six additional ionic salts used in this work and their effects on the energetic levels of the doped spiro-OMeTAD films. EDMPA, ethyldimethylpropylammonium; PMPIm, 3-methyl-1-propylpyridinium; BMIM, 1-propyl-3-methyl-imidazolium. (**C**) *J-V* curves of PSCs based on the spiro-OMeTAD HTL doped with six additional ionic salts (14 mol % radicals).

spiro-OMeTAD$^{\bullet+}$TFSI$^-$ radical that decreased the spin lifetime (*50*).

We further investigated the impact of these Coulomb interactions on the frontier orbital energies by combining the photoelectron spectroscopy data and DFT results. The incorporation of TBMP$^+$TFSI$^-$ not only decreased the energy offset between the HOMO level and the Fermi level but also changed the density of states (DOS) of frontier orbitals (Fig. 3D). In addition, low-energy inverse photoelectron spectra (LEIPS) indicated that the SUMO level of spiro-OMeTAD$^{\bullet+}$ downshifted from −4.06 to −4.30 eV upon addition of TBMP$^+$TFSI$^-$ (fig. S33). The DFT calculations highlighted the effect of the ionic salt on the molecular orbital levels (figs. S34 and S35), which we rationalized by considering that the TBMP$^+$TFSI$^-$ ionic salt screened the Coulomb attraction between the counterion and hole polaron in the spiro-OMeTAD$^{\bullet+}$TFSI$^-$ complex (*51*). In this context, the impact of the TBMP$^+$TFSI$^-$ can be viewed as a modulation of the activation energy of doping (E_a^d) related to the energy difference between the doping states and transport states (Fig. 3E), because neutral spiro-OMeTAD molecules close to TFSI$^-$ anions from the ionic salts can homogenize the electrostatic potential of the transport states, resulting in decreased E_a^d and increased WF.

Given this understanding of the impact of ionic salts on the energetic levels, we investigated why there was no conductivity enhancement with increasing WF, a feature that makes it decouple conductivity and WF tuning. Decreasing the E_a^d of dopants upon ionic salt addition (Fig. 3E) enabled an increasing fraction of hole polarons to be thermally populated. This effect, taken alone, would lead to a conductivity increase. However, the temperature-dependent conductivity indicated that the ionic salts also increase disorder. The temperature-dependent conductivity measurements revealed a faster-decreasing rate of conductivity upon addition of TBMP$^+$TFSI$^-$ and suggested an increased long-distance intermolecular charge hopping potential barrier (E_a^h) from 0.14 eV to 0.20 eV (*52*, *53*) (Fig. 3F and fig. S36). This more difficult long-distance intermolecular charge transfer implied a decreased mobility that might be induced by increased disorder or more scattering from ionic clusters (*54*, *55*). Overall, the ionic salts played a dual role: They increased the free hole population but also increased disorder. These two effects largely compensated each other and led to negligible conductivity changes over a broad range of ionic salt concentrations.

The generality of the IM radical doping strategy

Stimulated by the possibilities of precise energetic manipulation and facile conductivity tunability, we applied the IM radical doping approach to perovskites with different compositions and devices with different architectures (planar or mesoporous structures). In addition to the PSCs based on SnO_2/$(FAPbI_3)_{0.99}(MAPbBr_3)_{0.01}$ and TiO_2/$FAPbI_3$ shown in Fig. 1, B and C, IM radical–doped spiro-OMeTAD HTLs also resulted in high PCEs in perovskites with different band gaps, different fabrication methods (one-step or two-step), and with or without ionic liquid additives. All PCEs were similar to (or slightly higher than) those based on conventionally doped spiro-OMeTAD HTL (Fig. 4A, fig. S37, and tables S4 and S5), indicating that our IM radical doping strategy is applicable to different PSCs. In addition, we observed improved stability (both under high RH and high temperature) for all the PSCs using IM radical–doped spiro-OMeTAD compared with those using conventionally doped spiro-OMeTAD (fig. S38).

The generality of the IM radical doping strategy was also demonstrated in terms of the ionic salts. We investigated six additional ionic salts, based on typical anions [bis(trifluoromethylsulfonyl)imide, hexafluorophosphate, tetrafluoroborate, p-toluenesulfonate] and cations (ethyldimethylpropylammonium, propylpyridinium, imidazolium, methylpyridinium) (Fig. 4B). All of the ionic salts could effectively tune the WF (Fig. 4B and fig. S39) without negatively affecting the conductivity (fig. S40). Their incorporation resulted in high V_{oc} values (~1.12 to

1.16 V) and high PCEs (~22% to 23%) in SnO_2/$(FAPbI_3)_{0.99}(MAPbBr_3)_{0.01}$-based PSCs (Fig. 4C and table S6). Although the use of different cations resulted in negligible WF modifications, we noted that switching from $TFSI^-$ to other anions could slightly decrease the WF, which pointed to the anions playing a more prominent role in the energetic modulation in the framework of the IM radical doping strategy. A possible reason is that the anions coming from the ionic salts can exchange with $TFSI^-$ in the radical complex, resulting in new radical complex species with different energetics.

Discussion

Because the energetics of the hole polarons are sensitive to their local ionic environment, the IM radical doping strategy provides room to manipulate the WF as a function of the nature of the ionic salts. WF tuning could be achieved over a large range by controlling the interaction strength between the ionic salts and the radical complex and is more easily adjustable than WF modulation through interfacial molecular dipoles (*46*). As such, the IM radical doping strategy fills the gap between several previous strategies to enhance WF and conductivity and greatly expands the toolbox for organic semiconductor doping (*56*, *57*).

REFERENCES AND NOTES

1. H. Min *et al*., *Nature* **598**, 444–450 (2021).
2. T. Zhang *et al*., *Joule* **2**, 2706–2721 (2018).
3. S. Bai *et al*., *Nature* **571**, 245–250 (2019).
4. S. Chen *et al*., *Nat. Sustain.* **4**, 636–643 (2021).
5. J. Xue *et al*., *Science* **371**, 636–640 (2021).
6. Y. H. Lin *et al*., *Science* **369**, 96–102 (2020).
7. A. Al-Ashouri *et al*., *Science* **370**, 1300–1309 (2020).
8. K. Xiao *et al*., *Nat. Energy* **5**, 870–880 (2020).
9. J. Jeong *et al*., *Nature* **592**, 381–385 (2021).
10. M. Jeong *et al*., *Science* **369**, 1615–1620 (2020).
11. J. J. Yoo *et al*., *Nature* **590**, 587–593 (2021).
12. M. Kim *et al*., *Joule* **3**, 2179–2192 (2019).
13. G. Kim *et al*., *Science* **370**, 108–112 (2020).
14. S. Wang *et al*., *Nano Lett.* **16**, 5594–5600 (2016).
15. U. B. Cappel, T. Daeneke, U. Bach, *Nano Lett.* **12**, 4925–4931 (2012).
16. R. L. Forward *et al*., *ACS Energy Lett.* **4**, 2547–2551 (2019).
17. S. G. Kim *et al*., *Adv. Mater.* **33**, e2007431 (2021).
18. A. K. Jena, M. Ikegami, T. Miyasaka, *ACS Energy Lett.* **2**, 1760–1761 (2017).
19. A. K. Jena, Y. Numata, M. Ikegami, T. Miyasaka, *J. Mater. Chem. A* **6**, 2219–2230 (2018).
20. J. Kong *et al*., *Nature* **594**, 51–56 (2021).
21. B. Xu *et al*., *ChemSusChem* **7**, 3252–3256 (2014).
22. J.-Y. Seo *et al*., *Energy Environ. Sci.* **11**, 2985–2992 (2018).
23. J.-Y. Seo *et al*., *Adv. Func. Mater.* **31**, 2102124 (2021).
24. A. Abate *et al*., *J. Am. Chem. Soc.* **135**, 13538–13548 (2013).
25. W. H. Nguyen, C. D. Bailie, E. L. Unger, M. D. McGehee, *J. Am. Chem. Soc.* **136**, 10996–11001 (2014).
26. B. Tan *et al*., *Adv. Energy Mater.* **9**, 1901519 (2019).
27. S. Wang *et al*., *J. Am. Chem. Soc.* **140**, 16720–16730 (2018).
28. F. Lamberti *et al*., *Chem* **5**, 1806–1817 (2019).
29. S. Fantacci, F. De Angelis, M. K. Nazeeruddin, M. Grätzel, *J. Phys. Chem. C* **115**, 23126–23133 (2011).
30. V. Coropceanu, M. Malagoli, J. M. André, J. L. Brédas, *J. Am. Chem. Soc.* **124**, 10519–10530 (2002).
31. W. Zhang *et al*., *Chem. Commun.* **56**, 1589–1592 (2020).
32. W. Zhang *et al*., *ACS Appl. Mater. Interfaces* **12**, 33751–33758 (2020).
33. J. You *et al*., *Nat. Nanotechnol.* **11**, 75–81 (2016).
34. W. Chen *et al*., *Science* **350**, 944–948 (2015).
35. Y. Hou *et al*., *Science* **358**, 1192–1197 (2017).
36. S. Olthof *et al*., *Phys. Rev. Lett.* **109**, 176601 (2012).
37. M. L. Tietze, P. Pahner, K. Schmidt, K. Leo, B. Lüssem, *Adv. Funct. Mater.* **25**, 2701–2707 (2015).
38. T. Koopmans, *Physica* **1**, 104–113 (1934).
39. R. A. Belisle, P. Jain, R. Prasanna, T. Leijtens, M. D. McGehee, *ACS Energy Lett.* **1**, 556–560 (2016).
40. P. Caprioglio *et al*., *Adv. Energy Mater.* **9**, 1901631 (2019).
41. M. Stolterfoht *et al*., *Energy Environ. Sci.* **12**, 2778–2788 (2019).
42. A. Fediai, F. Symalla, P. Friederich, W. Wenzel, *Nat. Commun.* **10**, 4547 (2019).
43. C. G. Tang *et al*., *Nature* **539**, 536–540 (2016).
44. Y. Yamashita *et al*., *Nature* **572**, 634–638 (2019).
45. N. Shibayama *et al*., *ACS Appl. Mater. Interfaces* **12**, 50187–50191 (2020).
46. Y. Zhou *et al*., *Science* **336**, 327–332 (2012).
47. Y. Li, H. Li, C. Zhong, G. Sini, J.-L. Brédas, *Npj Flex. Electron.* **1**, 1–8 (2017).
48. D. Shi *et al*., *Sci. Adv.* **2**, e1501491 (2016).
49. E. de Boer, C. MacLean, *J. Chem. Phys.* **44**, 1334–1342 (1966).
50. R. L. Ward, S. I. Weissman, *J. Am. Chem. Soc.* **76**, 3612 (1954).
51. R.-Q. Png *et al*., *Nat. Commun.* **7**, 11948 (2016).
52. N. Karl, *Synth. Met.* **133**, 649–657 (2003).
53. H. Abdalla, G. Zuo, M. Kemerink, *Phys. Rev. B* **96**, 241202 (2017).
54. P.-J. Chia *et al*., *Phys. Rev. Lett.* **102**, 096602 (2009).
55. K. Harada, F. Li, B. Maennig, M. Pfeiffer, K. Leo, *Appl. Phys. Lett.* **91**, 092118 (2007).
56. I. E. Jacobs, A. J. Moulé, *Adv. Mater.* **29**, 1703063 (2017).
57. C. Gaul *et al*., *Nat. Mater.* **17**, 439–444 (2018).

ACKNOWLEDGMENTS

We thank C. Bao for the help with temperature-dependent conductivity measurements; G. Zheng for help with the GIWAXS analysis; Y. Wang for help with the stability test; J. C. M. Yu for help with single-crystal characterization; and O. Inganäs, W. Xu, X. Liu, and X. Cai for valuable discussions. **Funding:** Supported by Swedish Research Council Vetenskapsrådet (grant 2018-04809), an ERC Starting Grant (717026), the Knut and Alice Wallenberg Foundation (Dnr KAW 2019.0082), and the Swedish Government Strategic Research Area in Materials Science on Functional Materials at Linköping University (Faculty Grant SFO-Mat-LiU 2009-00971). F.G. is a Wallenberg Academy Fellow. Work at the University of Arizona was funded by the UA College of Science and the Office of Naval Research, awards N00014-20-1-2110 and N00014-22-1-2379. Work at the École Polytechnique Fédérale de Lausanne was funded by Swiss National Science Foundation for financial support with project 200020_185041 and from the European Union's Horizon 2020 research and innovation program under grant agreement 764047. Work at Chiba University was funded by Advanced Low Carbon Technology Research and Development Program (ALCA) of Japan Science and Technology Agency (grant JPMJAL 1404). **Author contributions:** F.W. and F.G. conceived and supervised the project. T.Z., Z.H., F.W., and F.G. designed this project. Z.H. contributed to advising and providing chemistry solutions. T.Z., Z.H., and F.W. performed the investigations and analyzed the data. H.-B.K., I.W.C., and D.S.K. made the PSCs based on the meso-TiO_2. C.W., X.L., and M.F. conducted XPS and UPS measurements and analysis. E.C., V.C., and J.-L.B. conducted the DFT calculations and helped to discuss the doping mechanism. R.K., L.K., and J.B. performed NMR measurements. M.C. performed SEM measurements and helped with NMR interpretations. M.Y. and S.B. contributed to the discussions. Y.P. and W.M.C. performed EPR analysis. B.Y., J.S., and A.H. performed the MPP measurements. K.T. and H.Y. conducted the LEIPS measurements. S.-C.Y. and F.F. contributed to TOF-SIMS measurements. T.Z., F.W., and F.G. wrote the manuscript. All authors discussed the results and reviewed the manuscript. **Competing interests:** F.G., F.W., T.Z., and Z.H. have filed a patent based on the concept developed in this manuscript. They are also co-founders of the company LinXole AB, which commercializes the materials developed in this manuscript. The other authors declare no competing interests. **Data and materials availability:** All data are available in the main text or supplementary materials.

SUPPLEMENTARY MATERIALS

science.org/doi/10.1126/science.abo2757
Materials and Methods
Supplementary Text
Figs. S1 to S40
Tables S1 to S6
References (*58*–*66*)

Submitted 24 January 2022; accepted 22 June 2022
10.1126/science.abo2757

Science

Ion-modulated radical doping of spiro-OMeTAD for more efficient and stable perovskite solar cells

Tiankai ZhangFeng WangHak-Beom KimIn-Woo ChoiChuanfei WangEunkyung ChoRafal KonefalYuttapoom PuttisongKosuke TeradoLibor KoberaMengyun ChenMei YangSai BaiBowen YangJiajia SuoShih-Chi YangXianjie LiuFan FuHiroyuki YoshidaWeimin M. ChenJiri BrusVeaceslav CoropceanuAnders HagfeldtJean-Luc BrédasMats FahlmanDong Suk KimZhangjun HuFeng Gao

Science, 377 (6605), • DOI: 10.1126/science.abo2757

A radical doping approach

In perovskite solar cells, high power conversion efficiencies (PCEs) are usually obtained with an organic hole transporter called spiro-OMeTAD. This material must be doped to have sufficient conductivity and optimal work function, but the conventional process with lithium organic salts requires a long oxidation step that also affects device stability. Zhang *et al*. added spiro-OMeTAD biradical precursors that convert into stable organic monoradicals. Combined with ionic salts, this doping strategy formed solar cells with high PCEs (>25%) and improved stability. This approach also allows conductivity and work function to be tuned separately and could be applied in other optoelectronic devices. —PDS

Science (ISSN) is published by the American Association for the Advancement of Science. 1200 New York Avenue NW, Washington, DC 20005. The title *Science* is a registered trademark of AAAS.